Chemical Science

ROYAL SOCIETY OF CHEMISTRY

EDGE ARTICLE

View Article Online
View Journal

Cite this: DOI: 10.1039/d6sc01000h

All publication charges for this article have been paid for by the Royal Society of Chemistry

A thermochromic polyoxovanadate with a 200 000-fold conductivity gain for boosting zinc-ion battery performance

Ze-Xun Zhang,†[a] Xiao-Yue Zhang,†[a] Ping-Wei Cai,*[a] Shou-Tian Zheng*[a] and Cai Sun*[ab]

The performance of zinc-ion batteries is hampered by the cathode's limited Zn^{2+} intercalation capacity and sluggish kinetics. Herein, we propose, for the first time, a thermochromic charge-separation strategy that simultaneously enhances capacity, rate performance, and cycling stability. We synthesized a new organic–inorganic hybrid thermochromic polyoxovanadate (POV), $MV_2[H_2V_{10}O_{28}]$ (MV_2V_{10}, MV = methyl viologen cation) as a cathode, which undergoes thermo-induced electron transfer from O to V, accompanied by a color change from yellow to dark green, and the formation of an ultra-stable charge-separated state lasting over one year, as well as a transition from an insulator to a semiconductor with a 205 000-fold increase in electrical conductivity. After coloration, the capacity increased significantly by 57.3% from 172.8 to 271.8 mAh g^{-1} at 0.1 A g^{-1}, while also exhibiting remarkable rate performance with 61.1% retention at a 100-fold higher current density, and cycling stability with 97.6% retention over 6000 cycles at a high current density of 10 A g^{-1}. This work presents the first successful application of electron-transfer thermochromism to enhance ZIB performance, offering a promising strategy for the development of advanced cathode materials.

Received 4th February 2026
Accepted 24th March 2026

DOI: 10.1039/d6sc01000h

rsc.li/chemical-science

Introduction

Lithium-ion batteries face significant safety challenges due to flammable organic electrolytes and lithium dendrite-induced short circuits, despite their high theoretical capacity and dominant role in applications ranging from portable electronics to grid-scale storage.[1–4] Consequently, developing cost-effective, safe, high-capacity alternative battery technologies is imperative.[5–8] Aqueous zinc-ion batteries (ZIBs) have emerged as promising candidates for next-generation energy storage systems due to the advantages of low redox potential (−0.76 V *vs.* SHE), high safety, low cost, and high theoretical capacities (820 mAh g^{-1}).[9–11] As a critical component, cathode materials play a pivotal role in determining the overall performance of ZIBs. To date, the development of ZIB cathodes has been concentrated on manganese-based oxides,[12–14] vanadium-based compounds,[15–17] Prussian blue analogs,[18–20] iodine,[21,22] and organic materials.[23,24] Among them, vanadium oxides (VO_x) have been widely studied as cathodes for ZIBs because of their exceptional theoretical capacity and environmental friendliness.[25,26] However, the dissolution of VO_x in electrolytes seriously compromises cycling stability, leading to battery failure.[27,28] Compared to VO_x materials, the subclass polyoxovanadates (POVs) offer not only excellent redox capability *via* reversible multi-electron transfer[29] but also superior structural stability,[30] translating to higher cycling stability and lower solubility in electrolytes.

However, the limited intercalation capacity of Zn^{2+} ions in POVs results in a relatively low capacity compared to VO_x materials. Furthermore, the discrete nature of POV clusters impedes the establishment of efficient electron conduction pathways, leading to inherently low electronic conductivity, and consequently poor rate capacity. These two key limitations significantly hinder the broader application of POVs as cathode materials in ZIBs (Scheme 1a). Therefore, simultaneously enhancing both the capacity and rate performance of POV-based cathodes represents a critical and urgent challenge for their practical implementation.

If a POV exhibits charge-separated characteristics, it holds promise for simultaneously enhancing both the capacity and rate performance of ZIB cathodes. The additional electrons and holes of the charge-separated state can enhance performance in two key ways: (1) holes accommodate more electrons injected from the external circuit into the POV cathode and facilitate the insertion of more Zn^{2+} ions driven by these electrons, thereby increasing capacity; and (2) they act as charge carriers, boosting intrinsic conductivity and consequently improving rate

[a]*Fujian Provincial Key Laboratory of Advanced Inorganic Oxygenated-Materials, College of Chemistry, Fuzhou University, Fuzhou, Fujian 350108, China. E-mail: cai2022@fzu.edu.cn; stzheng@fzu.edu.cn; csun@fzu.edu.cn*

[b]*Fujian Science & Technology Innovation Laboratory for Optoelectronic Information of China, Fuzhou, Fujian 350108, China*

† These authors contributed equally to this work.

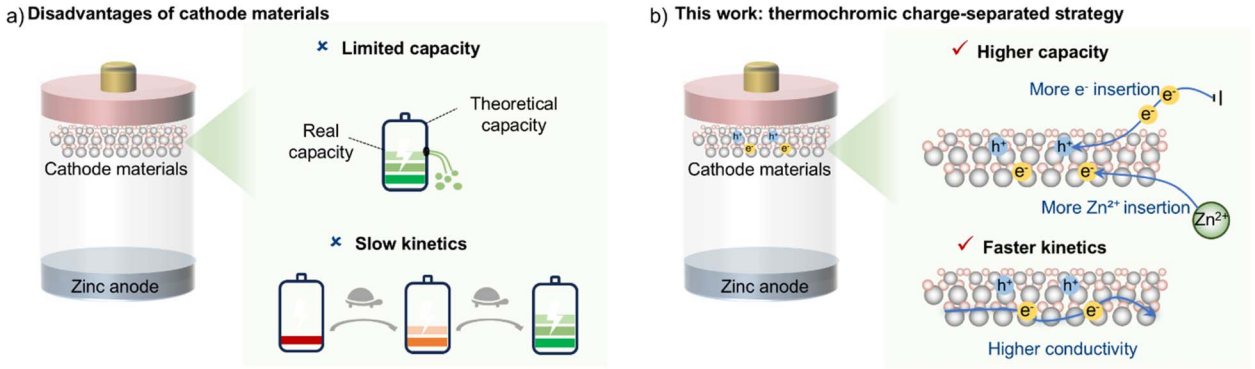

Scheme 1 (a) Schematic diagram of the ZIBs performance hampered by the cathode's limited capacity and slow kinetics; (b) proposed thermochromic charge-separation strategy to enhance ZIB performance.

performance. The key is to construct a stable charge-separated POV material with carrier channels (Scheme 1b).

Electron-transfer (ET) thermochromic materials have been reported to form charge-separated states.[31] Moreover, N-heterocyclic aromatic cations, particularly methyl viologen (MV^{2+}), can effectively stabilize these states through π-cation polarization effects.[32] Inspired by this, we synthesized a novel POV, $MV_2[H_2V_{10}O_{28}]$ (MV_2V_{10}), by incorporating MV as the countercation. MV_2V_{10} exhibits thermochromic properties and undergoes thermo-induced electron transfer (TIET) from O to V after heating, with the formation of an ultra-stable charge-separated state lasting over one year under ambient conditions. Interestingly, the observed conductivity ratio between the colored and initial samples reached 205 000-fold, representing a record for switchable bistable semiconductors.[33–38] The colored sample demonstrates excellent performance as a cathode material for ZIBs: (1) it delivers a high capacity of 271.8 mAh g^{-1} at 0.1 A g^{-1}, representing a 57.3% increase compared to the initial sample; (2) it retains 61.1% capacity at a 100-fold higher current density, significantly exceeding the 33.1% retention of the initial sample; (3) it exhibits outstanding long-term cyclability with 97.6% capacity retention after 6000 cycles at 10 A g^{-1}, substantially higher than the 83.4% observed for the initial sample. The colored sample also outperforms excellent vanadium-based compounds in ZIBs.[3,39–44] Systematic experimental results together with theoretical calculations reveal that the additional electrons and holes contribute to electrical energy storage and fast kinetics in ZIBs, thereby enhancing the specific capacity and rate performance. This is the first example of ET thermochromism to enhance ZIB performance.

Results and discussion

Crystal structure

Yellow block-shaped crystals of MV_2V_{10} were synthesized hydrothermally by reacting NH_4VO_3 and $MVCl_2$ in water at 120 °C for 3 days, with the pH adjusted to 5.5 using 2 M HCl. The phase purity of crystal MV_2V_{10} was examined by powder X-ray diffraction (PXRD, Fig. S1), Fourier transform infrared (FT-IR) spectroscopy (Fig. S2) and elemental analysis (EA, see the Experimental section in the SI). Single-crystal X-ray diffraction (SXRD) reveals that the molecular structure of MV_2V_{10}-a consists of an isolated $[H_2V_{10}O_{28}]^{4-}$ (V_{10}) polyanion cluster and two MV cations (Fig. 1a). The V_{10} is constructed from ten edge-sharing distorted VO_6 octahedra. There are 28 oxygen atoms, including 2 central oxygen atoms (O_c), 8 terminal oxygen atoms (O_t), 14 μ_2-bridging oxygen atoms (μ_2-O_b), and 4 μ_3-bridging oxygen atoms (μ_3-O_b). The proton resides on the O4 (μ_2-O) atom and further forms an O4–H···O5 hydrogen bond with the O5 (O_t) from another adjacent V_{10} cluster (Fig. 1b and S3), where d(H···O5) = 1.86 Å, indicating typical hydrogen bond interactions.[45] Adjacent clusters are bridged by two such hydrogen bonds along the a-axis, generating an infinitely extended hydrogen-bonded chain. Two MV cations act as counter cations, and the shortest distances from the N atom in MV to the center of the pyridine of adjacent MV cations are 4.02 Å and 4.85 Å, respectively, indicating negligible π–π interactions.[46]

Thermochromism

MV_2V_{10} displays thermochromic properties. The as-synthesized crystalline sample (MV_2V_{10}-a) changes color from yellow to dark green (MV_2V_{10}-b) after heating at 200 °C in air (inset of Fig. 1c). As shown in UV-Vis absorption spectra (Fig. 1c), MV_2V_{10}-a exhibits a distinct absorption edge at 580 nm, consistent with its yellow colour. After heating, a new absorption band emerges above 580 nm (Fig. 1c) and extends to 2500 nm (Fig. S4). The absorption intensity increases progressively with prolonged heating time, and the coloration tends to be saturated after 180 minutes of heating.

Thermogravimetry analysis (TGA, Fig. S5) indicates that MV_2V_{10} remains stable up to at least 200 °C. PXRD patterns (Fig. S1) and FT-IR spectroscopy (Fig. S2) demonstrate that MV_2V_{10}-b undergoes no significant structural changes during the coloration process, which is further corroborated by SXRD data (Tables S1 and S2). These results demonstrate that the coloration does not derive from thermally induced decomposition or structural isomerization.

Subsequently, no electron paramagnetic resonance (EPR) signal is detected for MV_2V_{10}-a, while characteristic unpaired electron signals are observed after coloration (Fig. 1d). The rhombic symmetry signal at $g_\perp = 1.98$ and $g_\parallel = 1.91$ clearly

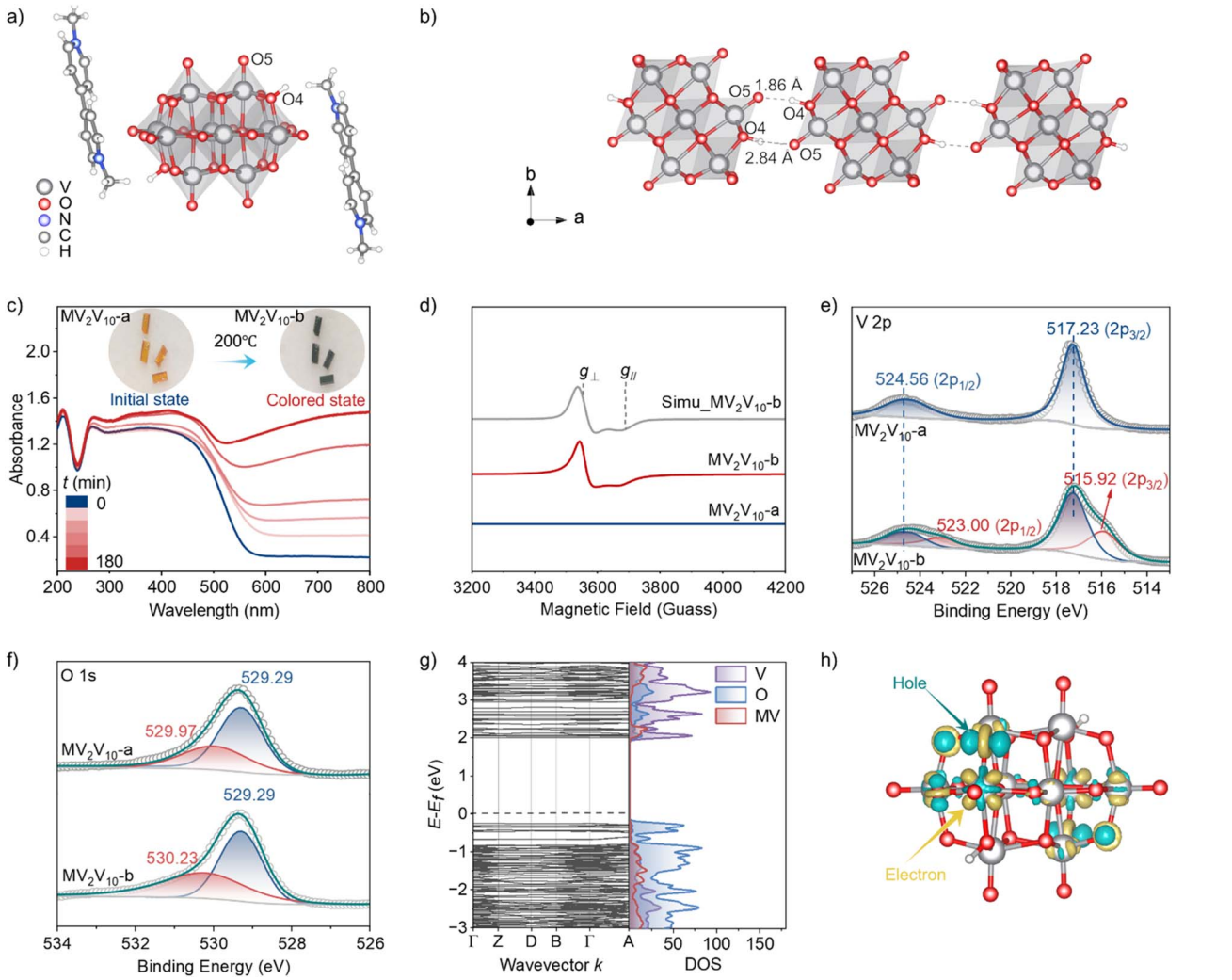

Fig. 1 For MV_2V_{10}. (a) Molecular structure; (b) V_{10} cluster chain connected by dual hydrogen bonds along the *a*-axis; (c) time-dependent UV-Vis spectra, inset: colour change after heating; (d) EPR spectra of MV_2V_{10}-a, MV_2V_{10}-b and simulated MV_2V_{10}-b, where [$g_\perp$, $g_\parallel = 1.98, 1.91$]; (e and f) XPS (Al-Kα) core level spectra of V 2p and O 1s. (g) BS (left) and DOS (right). The Fermi level is set to zero. (h) Electron density difference of the V_{10} structure, yellow and dark green colors represent charge accumulation and depletion after electron transfer, respectively.

confirms the presence of V^{IV}, confirming that the thermochromic mechanism originates from electron transfer. So, the thermo-induced absorption band above 580 nm can be attributed to V^{IV}-to-V^{V} intervalence charge transfer (IVCT). X-ray photoelectron spectroscopy (XPS, Fig. 1e and f) further confirms the electron transfer behavior. The V 2p core-level spectrum exhibits significant changes after coloration. Prior to coloration, V^{V} is characterized by peaks at approximately 517.23 eV ($2p_{3/2}$) and 524.56 eV ($2p_{1/2}$). After coloration, new peaks emerge at lower binding energies (515.92 eV for $2p_{3/2}$ and 523.00 eV for $2p_{1/2}$), attributed to the formation of partial V^{IV}, indicating V atoms acting as electron receptors. Concurrently, the initial O 1s peak at 529.29 eV is accompanied by a new peak at higher binding energy (530.23 eV), indicating O atoms acting as electron donors. Band structure (BS) and density of states (DOS) calculations reveal a bandgap of ~2.25 eV (Fig. 1g, S6 and S7). The valence band maximum (VBM) is predominantly composed of O 2p orbitals, while the conduction band minimum (CBM) consists primarily of V 3d orbitals, suggesting favorable electronic transfer from O to V sites. Electron density difference ($\Delta\rho$) isosurfaces (Fig. 1h) clearly visualize electron transfer from bridging oxygen atoms (O_b) to adjacent V atoms, localizing holes on O_b and confirming the charge-separated state. This is further corroborated by calculated ADCH and Hirshfeld charges, which show increased positive charge on O_b and increased negative charge on adjacent V atoms in the charge-separated state (Fig. S8 and Table S3). Remarkably, MV_2V_{10}-b exhibits a long-lived charge-separated state that remains stable for over one year under ambient conditions (Fig. S9). This exceptional stability is mainly due to the strong π-cation polarization effect of the MV, which effectively stabilizes the charge-separated state of the V_{10} cluster.[32]

Electrical conductivity

Bulk electrical properties of MV_2V_{10} were measured using a lateral device configuration *via* the two-probe method with

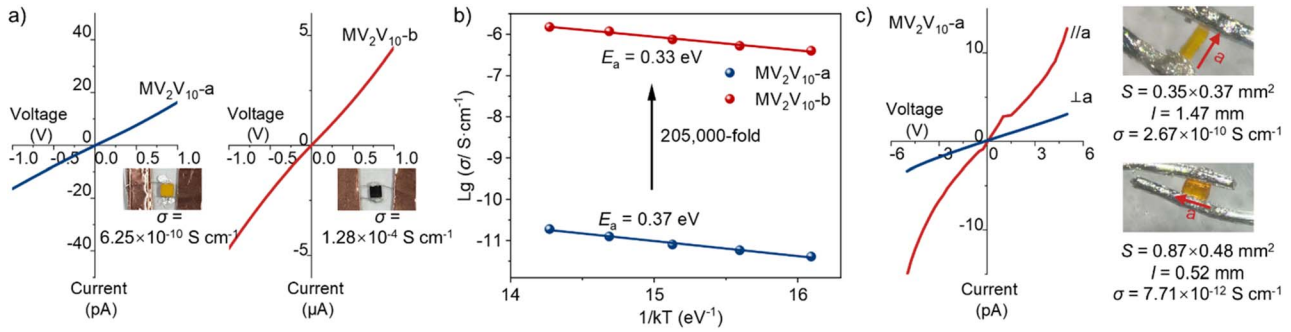

Fig. 2 (a) *I–V* curves of pellet sample MV_2V_{10}-a and MV_2V_{10}-b, inset: photographs of the two-probe electrical test method. (b) Arrhenius plots. E_a is the activation energy. (c) *I–V* curves and photographs of single crystal sample MV_2V_{10}-a, along (∥*a*) and perpendicular (⊥*a*) to the *a*-axis.

silver paste contacts at room temperature (Fig. 2a and S10). Pellet samples of both MV_2V_{10}-a and MV_2V_{10}-b exhibit ohmic current–voltage (*I–V*) characteristics. Remarkably, the electrical conductivity increases by five orders of magnitude (205 000-fold) from an insulating level (6.25×10^{-10} S cm^{-1}) to a semiconducting level (1.28×10^{-4} S cm^{-1}) after coloration. To our knowledge, this represents the highest conductivity contrast reported to date for switchable bistable semiconductors (Table S4). The linear relationship between the natural logarithm of σ *versus* $1/T$ reveals a decrease in activation energy (E_a) from 0.37 to 0.33 eV after coloration, indicating an increase in carrier density (Fig. 2b).[38] Hall effect measurements further confirm n-type semiconducting behavior in MV_2V_{10}-b, revealing a carrier concentration of 1.01×10^{14} cm^{-3} and mobility of 2.65 cm^2 V^{-1} s^{-1} (Table S5). Notably, the carrier concentration in MV_2V_{10}-b exceeds that of commercial semiconductors (*e.g.*, Si, Ge, GaAs) (Table S6).[47] To elucidate the origin of the conductivity enhancement, anisotropic conductivity measurements were performed on single crystals of MV_2V_{10}. The results reveal a 35-fold higher conductivity along the *a*-axis direction compared to the perpendicular direction, indicating preferential carrier transport along the *a*-axis (Fig. 2c and S11). This suggests that carriers generated by TIET are not localized on individual V_{10} clusters but likely migrate *via* the dual O4–H···O5 hydrogen bonds between adjacent V_{10} clusters along the *a*-axis.

Electrochemical performances of ZIBs

Motivated by the ultra-stable charge-separated state and huge conductivity enhancement (Fig. 2a and S12) of MV_2V_{10} after coloration, as well its stability in the electrolyte (Fig. S13), we further evaluated its zinc storage performance as a cathode material for aqueous ZIBs. Fig. 3a shows the configuration of the ZIBs. Fig. 3b and S14 display the cyclic voltammetry (CV) curves. For MV_2V_{10}-a, only a distinct reduction peak is observed in the first CV scan, whereas MV_2V_{10}-b displays two reduction peaks (V^{5+} to V^{4+} and V^{4+} to V^{3+}), indicating stronger redox activity of MV_2V_{10}-b.[48] The slight peak shifts between the first and second scans facilitate charge transfer and lower the electrochemical energy barrier.[49] The pronounced current at 0.2 V and overlapping features near 1.9 V in MV_2V_{10}-b indicate the formation of a stable cathode electrolyte interphase, which suppresses vanadium dissolution.[50] Moreover, the MV_2V_{10}-b cathode exhibits a larger CV integral area (1.34) compared to MV_2V_{10}-a (0.61, Fig. 3c), indicating a higher specific capacity. The galvanostatic charge–discharge (GCD) curves at a low current density of 0.1 A g^{-1} (Fig. 3d) demonstrate that the MV_2V_{10}-b cathode shows a higher capacity of 271.8 mAh g^{-1} compared to that of MV_2V_{10}-a (172.8 mAh g^{-1}), with a decent cycle life and a coulombic efficiency of nearly 100% after 200 cycles (Fig. S15 and S16).

The rate performance of the MV_2V_{10} cathode is depicted in Fig. 3e and S17, where MV_2V_{10}-b shows superior rate capacities compared to MV_2V_{10}-a. The MV_2V_{10}-b delivers average capacities of 270.3, 267.6, 252.0, 234.9, 217.5, and 186.0 mAh g^{-1} at 0.1, 0.2, 0.5, 1, 2, and 5 A g^{-1}, respectively. Even under a 100-fold increase in current density from 0.1 to 10 A g^{-1}, MV_2V_{10}-b maintains 61.1% of its capacity (165.2 mAh g^{-1}), which is attributed to its 205 000-fold conductivity gain. Upon returning to 2.0 A g^{-1}, the capacity of MV_2V_{10}-b recovers to 215.3 mAh g^{-1}. In contrast, MV_2V_{10}-a undergoes a more rapid capacity decay at 0.2 A g^{-1}, likely due to more severe dissolution, and retains only 33.1% of its capacity under the same 100-fold current density increase, significantly lower than that of MV_2V_{10}-b. Additionally, MV_2V_{10}-b shows lower polarization compared to MV_2V_{10}-a at various current densities (Fig. S18).

The MV_2V_{10}-b cathode demonstrates a remarkable capacity retention of 100% at 2 A g^{-1} after 1000 cycles (Fig. 3f), which is superior to 87.7% of the MV_2V_{10}-a electrode. Taken together, these data verify that the significantly improved cycling stability is attributed to the giant conductivity gain of MV_2V_{10}-b, which preserves the structural integrity of the electrode by suppressing irreversible damage during Zn^{2+} intercalation/deintercalation.

The dQ/dV plots, a useful indicator of cycling stability and polarization,[41] reveal greater curve overlap and a smaller polarization gap for MV_2V_{10}-b *versus* MV_2V_{10}-a (Fig. S19), suggesting reduced polarization and enhanced cycling stability. Furthermore, the long-term stability at a high current density of 10 A g^{-1} was also evaluated (Fig. 3g), where the MV_2V_{10}-b cathode delivers a highly reversible capacity of 142.3 mAh g^{-1} after 6000 cycles, exhibiting a high-capacity retention rate of 97.6% and an ultralow capacity fading rate of 0.0004% per cycle, much higher than that of the MV_2V_{10}-a cathode, even surpassing many recently reported VO_x materials (Fig. 3h and

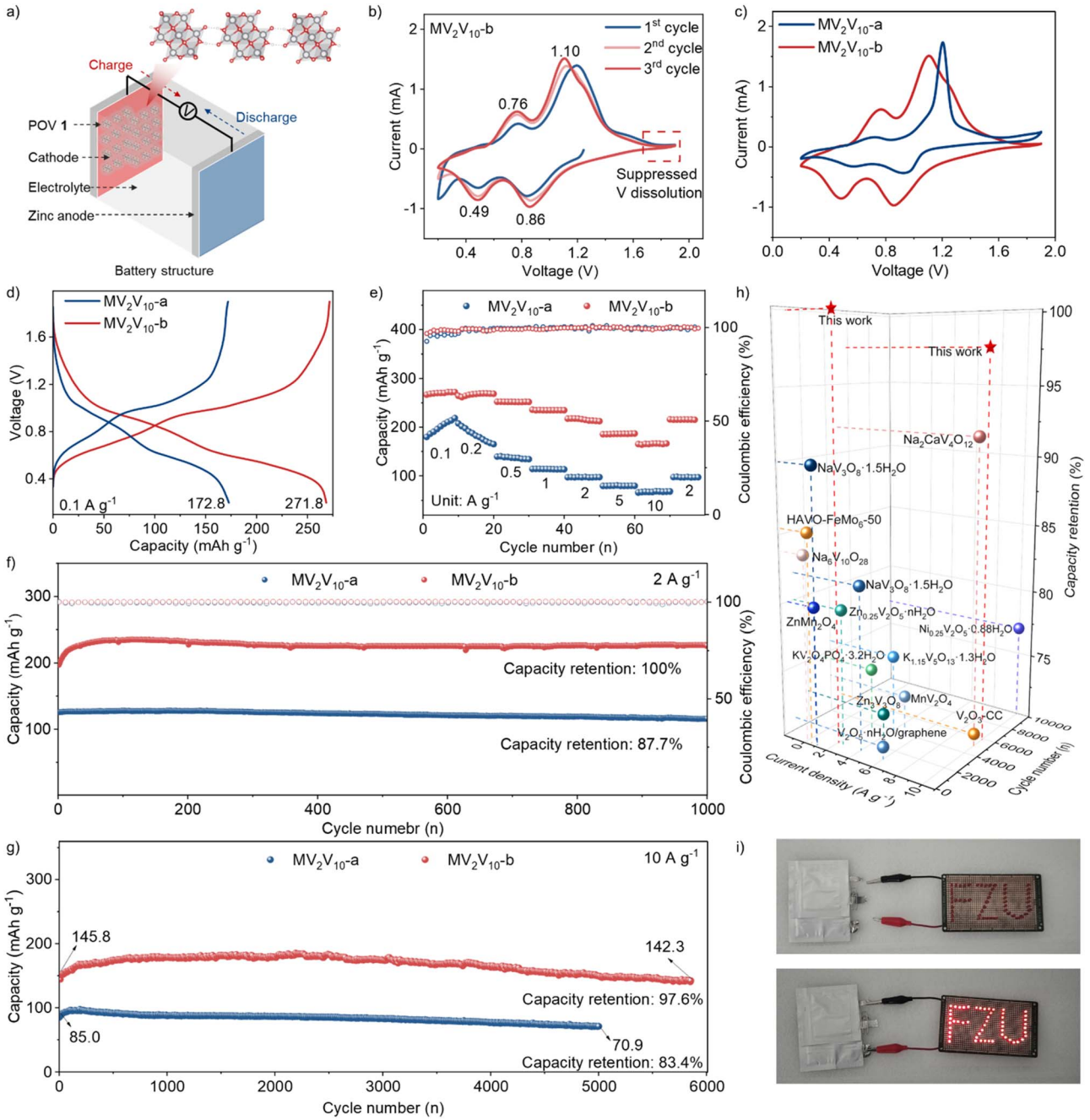

Fig. 3 (a) Schematic diagram of the battery configuration with POV **1** as the cathode and zinc as the anode. (b) CV curves of the MV_2V_{10}-b electrode for the first three cycles at a scan rate of 1.0 mV s^{-1} within a voltage range of 0.2–1.9 V (0.2 → 1.9 V represents zinc extraction, 1.9 → 0.2 V represents zinc insertion). (c) CV curves at the third cycle; (d) cycling performance at 0.1 A g^{-1}; (e) rate capability curves at 0.2–10 A g^{-1}; (f) cycling performance at 2 A g^{-1}; (g) cycling performance of MV_2V_{10}-a and MV_2V_{10}-b cathodes at 10 A g^{-1}. (h) The comparison of cycling stability between this work and other previous reports (data sources: Table S7). (i) Digital photograph of red LEDs powered by a soft pack battery (3 × 3 cm^{-2}) in the flat state, consisting of an MV_2V_{10}-b cathode and a zinc foil anode.

Table S7). As shown in Fig. S20, the τ_2 peak (~10^{-3} to 10^{-2} s) arises from ion adsorption/desorption at the electrode surface and the charge transfer process. In comparison to MV_2V_{10}-a, the lower impedance contribution and rapid peak attenuation in MV_2V_{10}-b point to superior interfacial reaction kinetics, attributed to the formation of charge-separated states, which significantly accelerates the transport of Zn^{2+}. To demonstrate practical availability, coin cells and soft-pack batteries employing the MV_2V_{10}-b cathode were fabricated. These devices successfully power a digital timer for 60 minutes (Fig. S21). Notably, the soft-pack batteries maintain operation under 0° and 180° bending conditions (Fig. 3i and S22), confirming exceptional flexibility and mechanical robustness.

To investigate the electrochemical reaction kinetics of the MV_2V_{10} cathode, the pseudocapacitive charge storage and diffusion control process were evaluated using CV curves at

different scan rates (Fig. 4a and S23). The calculated *b*-values for MV_2V_{10}-a and MV_2V_{10}-b electrodes are between 0.5 and 1 (Fig. 4b and S24), indicating that the Zn^{2+} storage behaviors are governed by a combination of diffusion and capacitive mechanisms. For the MV_2V_{10}-b cathode, the capacitive contribution gradually increases from 56.6% to 76.5% as the scan rate rises from 0.2 to 1 mV s^{-1} (Fig. 4c and S25). In contrast, the MV_2V_{10}-a cathode consistently exhibits lower capacitive contributions across all scan rates (Fig. S26 and S27), indicating superior charge transfer kinetics in the MV_2V_{10}-b cathode, primarily accounting for its enhanced rate capability. The adsorption energies of Zn^{2+} on the V_{10} surface in both the pristine and colored states were evaluated using density functional theory (DFT) calculations. The results demonstrate that the charge-separated state significantly enhances the adsorption energy of Zn^{2+} by approximately 0.15 eV (Fig. S28), thereby increasing the contribution to the surface capacitance. Moreover, the MV_2V_{10}-b cathode demonstrates lower impedance than MV_2V_{10}-a across various voltages (Fig. S29 and S30), indicating superior charge transfer kinetics and enhanced electrochemical activity. We further calculated the E_a values using the Arrhenius equation at different voltages (Fig. S31). As shown in Fig. 4d, the E_a values of the MV_2V_{10}-b cathode were significantly lower than those of the MV_2V_{10}-a cathode across all voltages, indicating more favorable thermodynamics of the Zn^{2+} ion adsorption and desorption process, which is conducive to the overall performance of ZIBs. The galvanostatic intermittent titration technique (GITT) was employed to assess the ion diffusion kinetics during the charge and discharge processes (Fig. 4e). The Zn^{2+} diffusion coefficients ($D_{Zn^{2+}}$) for the MV_2V_{10}-b cathode were calculated to range from 10^{-9} to 10^{-11} cm^2 s^{-1} during various stages of zinc insertion/extraction, which are generally higher than those of the MV_2V_{10}-a electrode (Fig. 4f), indicating faster reaction kinetics of the MV_2V_{10}-b cathode, thereby contributing to superior rate performance.

To elucidate the zinc storage mechanism of the MV_2V_{10}-b cathode, *ex situ* XPS and XRD were conducted. The V 2p XPS results (Fig. 4g) reveal that V^{5+} and V^{4+} are predominant in the

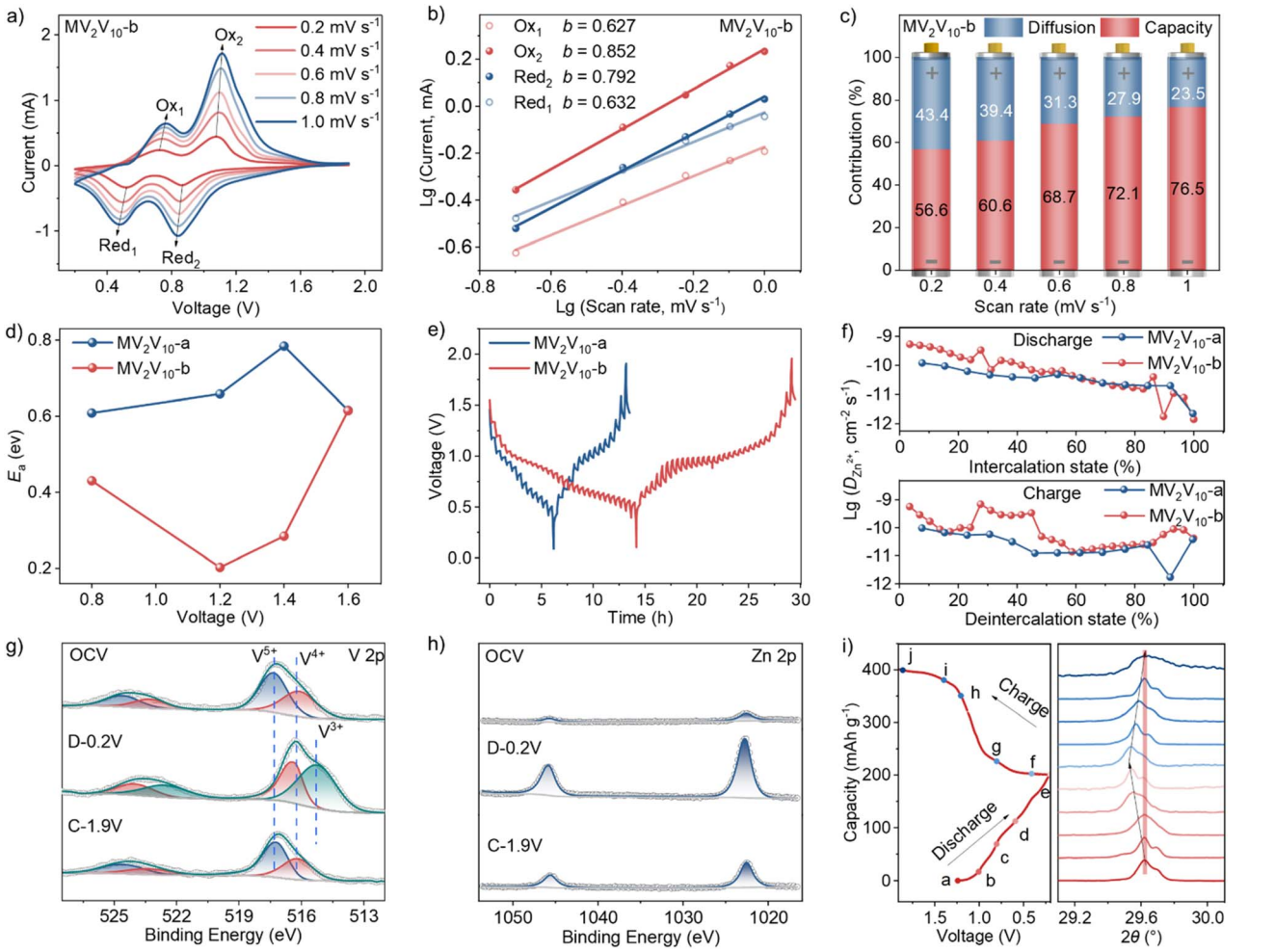

Fig. 4 (a) CV curves of MV_2V_{10}-b at different scan rates from 0.2 to 1.0 mV s^{-1}. (b) Plots of log(*i*) *vs.* log(*v*) of MV_2V_{10}-b at the four peaks shown in (a). (c) Capacity contribution ratios at different scan rates for MV_2V_{10}-b. (d) Activation energies at different voltages; (e) charge/discharge profiles measured using GITT; (f) corresponding Zn^{2+} diffusion coefficient (*D*) in the discharge (top)/charge (bottom) process of MV_2V_{10}-a and MV_2V_{10}-b cathodes (the abnormal $D_{Zn^{2+}}$ observed for the MV_2V_{10}-b sample at 90% depth of discharge was caused by the rapid voltage change). (g and h) *Ex situ* XPS of V 2p and Zn 2p for MV_2V_{10}-b at OCV, discharging at 0.2 V at 2nd, and charging 1.9 V at 3rd; (i) *ex situ* XRD patterns of MV_2V_{10}-b.

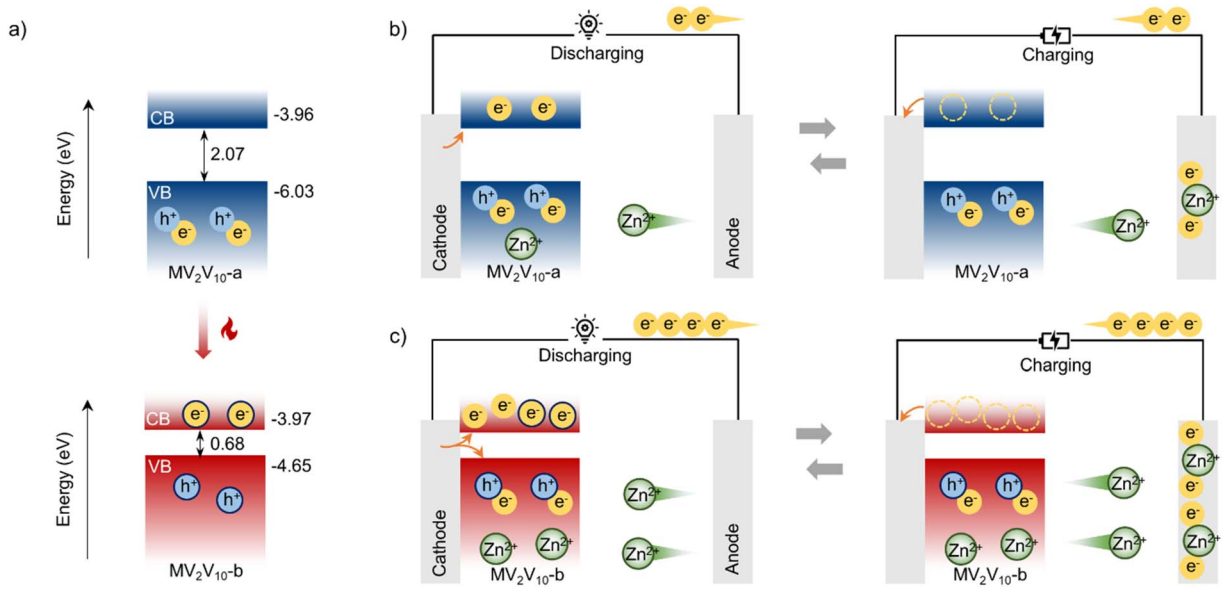

Fig. 5 (a) Schematic diagrams of the band structure. (b and c) Schematic illustration of the discharging/charging process demonstrating the mechanism of capacity enhancement for MV_2V_{10}-b. Note: the electrons and holes of the charge-separated state are outlined in blue.

pristine state (at open circuit voltage, OCV). Upon discharge to 0.2 V, the V^{5+} peak disappears, and V^{4+} and V^{3+} become dominant. Upon recharging to 1.9 V, the valence states of V revert to initial distribution. These results indicate that the zinc storage mechanism at the MV_2V_{10}-b cathode is mainly governed by the reversible redox pairs of V^{4+}/V^{5+} and V^{3+}/V^{4+}. Moreover, two prominent Zn 2p XPS peaks at 1022.48 eV and 1045.62 eV (Fig. 4h) during discharge to 0.2 V confirm successful Zn^{2+} insertion into the MV_2V_{10}-b cathode. Moreover, the characteristic diffraction peak (Fig. 4i) at 29.6° shifts to a lower angle when discharged to 0.2 V, indicating effective Zn^{2+} insertion. Upon charging to 1.9 V, the peak returns to a higher angle, confirming the reversible Zn^{2+} intercalation and the excellent structural stability of the MV_2V_{10}-b cathode. In other words, the lattice parameters remain unchanged. This may be ascribed to the fact that the increased carrier concentration reduces the electrostatic repulsion during Zn^{2+} intercalation and expands the transport pathways for Zn^{2+}.

Based on these results, we propose a phenomenological mechanism for the enhanced capacity after coloration (Fig. 5), and gaps and energy level alignments (*vs.* vacuum) for MV_2V_{10}-a and MV_2V_{10}-b (Fig. 5a) were determined using UV-Vis-NIR spectra (Fig. S4) and CV curves (Fig. S32 and Table S8). For the MV_2V_{10}-a electrode (Fig. 5b), Zn^{2+} ions are stripped from the Zn anode and intercalated into the cathode during discharge, while electrons flow through the external circuit into its CB. Upon charging, the process reverses, Zn^{2+} ions deintercalate from the MV_2V_{10}-a cathode and plate back onto the Zn anode, accompanied by the oxidation of MV_2V_{10}-a and electron extraction from the CB. In contrast, when MV_2V_{10}-b serves as the cathode (Fig. 5c), it exists in a stable charge-separated state with electrons occupying the CB and holes residing in the VB. During discharge, as electrons flow into the CB of MV_2V_{10}-b *via* the external circuit, partial recombination of additional electrons with holes occurs in the VB, thus enabling enhanced Zn^{2+} intercalation into the MV_2V_{10}-b electrode. During charging, MV_2V_{10}-b releases more electrons from its CB than MV_2V_{10}-a, along with deintercalation of more Zn^{2+} ions, thereby leading to an increased charge capacity. Notably, this additional capacity is reversibly delivered during the subsequent discharge cycle. As the extra holes are consumed by recombination in the first cycle, subsequent discharge processes exclusively involve electron injection into the CB. This mechanism consistently sustains the high specific capacity of the MV_2V_{10}-b cathode during extended cycling.

Conclusions

In summary, we have provided a thermochromic charge-separation strategy that can effectively enhance the capacity, rate performance, and cycling stability of ZIBs, outperforming excellent vanadium-based cathodes. The stable charge-separated state in MV_2V_{10} not only enhances electronic conductivity by 205 000-fold through dual hydrogen-bonded inter-cluster pathways, thereby accelerating reaction kinetics, and enabling excellent rate performance, but also provides additional electrons and holes, synergistically contributing to higher capacity. This work demonstrates the first example of enhanced ZIB performance induced by electron-transfer thermochromism, offering new insights into strategies for developing high-performance cathodes for ZIBs.

Author contributions

C. Sun and Z. X. Zhang conceived the idea, designed the experiments and co-wrote the paper. Z. X. Zhang performed material synthesis, material characterization, and electro-

chemistry measurement. X. Y. Zhang, P. W. Cai and S. T. Zheng discussed the results and revised the manuscript.

Conflicts of interest

The authors declare no conflict of interest.

Data availability

Supplementary information (SI): crystal and structure refinement data, FT-IR spectra, PXRD patterns, thermogravimetric analysis, UV-visible absorption spectra, electronic structure analysis, Zn ion battery data and calculated details. See DOI: https://doi.org/10.1039/d6sc01000h.

CCDC 2472756 (MV_2V_{10}-a) and 2485510 (MV_2V_{10}-b) contain the supplementary crystallographic data for this paper.[51a,b]

Acknowledgements

This work was supported by the National Natural Science Foundation of China (22371045, 22371046, and 22575052), and Fujian Provincial Natural Science Foundation (2025J01430 and 2025J09058).

References

1 K. W. Nam, H. Kim, Y. Beldjoudi, T.-w. Kwon, D. J. Kim and J. F. Stoddart, *J. Am. Chem. Soc.*, 2020, **142**, 2541–2548.
2 X. Tian, Q. Zhao, M. Zhou, X. Huang, Y. Sun, X. Duan, L. Zhang, H. Li, D. Su, B. Jia and T. Ma, *Adv. Mater.*, 2024, **36**, 2400237.
3 D. Kundu, B. D. Adams, V. Duffort, S. H. Vajargah and L. F. Nazar, *Nat. Energy*, 2016, **1**, 16119.
4 X. Shi, J. Xie, J. Wang, S. Xie, Z. Yang and X. Lu, *Nat. Commun.*, 2024, **15**, 302.
5 Y. Chen, Z.-X. Zhang, P.-W. Cai, Z.-W. Guo, Z.-W. Lu, C. Sun, X.-X. Li, J.-X. Chen, Z.-H. Wen and S.-T. Zheng, *Angew. Chem., Int. Ed.*, 2025, **64**, e202420284.
6 H. Dai, T. Sun, J. Zhou, J. Wang, Z. Chen, G. Zhang and S. Sun, *Nat. Commun.*, 2024, **15**, 8577.
7 J. Hao, L. Yuan, C. Ye, D. Chao, K. Davey, Z. Guo and S. Z. Qiao, *Angew. Chem., Int. Ed.*, 2021, **60**, 7366–7375.
8 P. Cai, W. Sun, J. Chen, K. Chen, Z. Lu and Z. Wen, *Adv. Energy Mater.*, 2023, **13**, 2301279.
9 S. Bi, S. Wang, F. Yue, Z. Tie and Z. Niu, *Nat. Commun.*, 2021, **12**, 6991.
10 Z. Zha, D. Li, T. Sun, Q. Sun, J. Hou, Z. Tao and J. Chen, *J. Am. Chem. Soc.*, 2024, **146**, 31612–31623.
11 X. Yu, Z. Li, X. Wu, H. Zhang, Q. Zhao, H. Liang, H. Wang, D. Chao, F. Wang, Y. Qiao, H. Zhou and S.-G. Sun, *Joule*, 2023, **7**, 1145–1175.
12 M. Li, C. Liu, J. Meng, P. Hei, Y. Sai, W. Li, J. Wang, W. Cui, Y. Song and X. X. Liu, *Adv. Funct. Mater.*, 2024, **34**, 2405659.
13 J. Liang, Y. Zhao, L. Ren, M. Li, Q. Zhang, Y. Wang, X. Sun, M. Chuai, X. Wang and W. Liu, *Adv. Funct. Mater.*, 2025, **35**, 2501135.
14 Y. Ding, C. Cai, L. Ma, J. Wang, M. P. Mercer, J. Liu, D. Kramer, X. Yu, D. Xue, C. Zhi and C. Peng, *Adv. Energy Mater.*, 2024, **15**, 2402819.
15 N. Qiu, Z. Yang, Y. Wang, Y. Zhu and W. Liu, *Chem. Commun.*, 2020, **56**, 9174–9177.
16 Q. Zhang, S. Ju, S. Zhang, S. Xu and Z. Zhang, *Adv. Energy Mater.*, 2025, **15**, 2404597.
17 G. Yuan, Y. Su, X. Zhang, B. Gao, J. Hu, Y. Sun, W. Li, Z. Zhang, M. Shakouri and H. Pang, *Natl. Sci. Rev.*, 2024, **11**, nwae336.
18 Y. Zeng, X. F. Lu, S. L. Zhang, D. Luan, S. Li and X. W. Lou, *Angew. Chem., Int. Ed.*, 2021, **60**, 22189–22194.
19 Y. Liu, X. Zhou, T. Qiu, R. Yao, F. Yu, T. Song, X. Lang, Q. Jiang, H. Tan, Y. Li and Y. Li, *Adv. Mater.*, 2024, **36**, 2407705–2407715.
20 Q. Yang, F. Mo, Z. Liu, L. Ma, X. Li, D. Fang, S. Chen, S. Zhang and C. Zhi, *Adv. Mater.*, 2019, **31**, 1901521.
21 S.-J. Zhang, J. Hao, H. Wu, Q. Chen, Y. Hu, X. Zhao and S.-Z. Qiao, *J. Am. Chem. Soc.*, 2025, **147**, 16350–16361.
22 J.-L. Yang, H.-H. Liu, X.-X. Zhao, X.-Y. Zhang, K.-Y. Zhang, M.-Y. Ma, Z.-Y. Gu, J.-M. Cao and X.-L. Wu, *J. Am. Chem. Soc.*, 2024, **146**, 6628–6637.
23 X. Guo, H. Xu, Y. Tang, Z. Yang, F. Dou, W. Li, Q. Li and H. Pang, *Adv. Mater.*, 2024, **36**, 2408317.
24 H. Hong, Y. Wang, Z. Wei, X. Yang, Z. Wu, X. Guo, A. Chen, S. Zhang, S. Wang, Q. Li, S. Li, D. Zhang, Q. Xiong and C. Zhi, *Adv. Mater.*, 2024, **36**, 2410209.
25 F. Wan, L. Zhang, X. Dai, X. Wang, Z. Niu and J. Chen, *Nat. Commun.*, 2018, **9**, 1656.
26 X. Chen, H. Zhang, J.-H. Liu, Y. Gao, X. Cao, C. Zhan, Y. Wang, S. Wang, S.-L. Chou, S.-X. Dou and D. Cao, *Energy Storage Mater.*, 2022, **50**, 21–46.
27 K. Zhu and W. Yang, *Acc. Chem. Res.*, 2024, **57**, 2887–2900.
28 Y. Kim, Y. Park, M. Kim, J. Lee, K. J. Kim and J. W. Choi, *Nat. Commun.*, 2022, **13**, 2371.
29 Y. Huang, J. Hu, H. Xu, W. Bian, J. Ge, D. Zang, D. Cheng, Y. Lv, C. Zhang, J. Gu and Y. Wei, *Adv. Energy Mater.*, 2018, **8**, 1800789.
30 T. Zhou, L.-L. Xie, Y. Niu, H.-R. Xiao, Y.-J. Li, Q. Han, X.-J. Qiu, X.-L. Yang, X.-Y. Wu, L.-M. Zhu, H. Pang and X.-Y. Cao, *Rare Met.*, 2023, **42**, 1431–1445.
31 Y. F. Sang, H. Zeng, L. J. Xu and Z. N. Chen, *Adv. Funct. Mater.*, 2022, **32**, 2206459.
32 D. H. Li, X. Y. Zhang, J. Q. Lv, P. W. Cai, Y. Q. Sun, C. Sun and S. T. Zheng, *Angew. Chem., Int. Ed.*, 2023, **62**, e202312706.
33 I. Chung, J.-H. Song, J. Im, J. Androulakis, C. D. Malliakas, H. Li, A. J. Freeman, J. T. Kenney and M. G. Kanatzidis, *J. Am. Chem. Soc.*, 2012, **134**, 8579–8587.
34 S. Roy, S. P. Mondal, S. K. Ray and K. Biradha, *Angew. Chem., Int. Ed.*, 2012, **51**, 12012–12015.
35 C. Jia, A. Migliore, N. Xin, S. Huang, J. Wang, Q. Yang, S. Wang, H. Chen, D. Wang, B. Feng, Z. Liu, G. Zhang, D.-H. Qu, H. Tian, M. A. Ratner, H. Q. Xu, A. Nitzan and X. Guo, *Science*, 2016, **352**, 1443–1445.
36 C. Sun, M. S. Wang, P. X. Li and G. C. Guo, *Angew. Chem., Int. Ed.*, 2017, **56**, 554–558.

37 C. Sun, G. Xu, X.-M. Jiang, G.-E. Wang, P.-Y. Guo, M.-S. Wang and G.-C. Guo, *J. Am. Chem. Soc.*, 2018, **140**, 2805–2811.
38 C. Sun, X. Q. Yu, M. S. Wang and G. C. Guo, *Angew. Chem., Int. Ed.*, 2019, **58**, 9475–9478.
39 Q. Zhang, S. Ju, S. Zhang, S. Xu and Z. Zhang, *Adv. Energy Mater.*, 2025, **15**, 2404597.
40 N. Zhang, F. Cheng, Y. Liu, Q. Zhao, K. Lei, C. Chen, X. Liu and J. Chen, *J. Am. Chem. Soc.*, 2016, **138**, 12894–12901.
41 D. Li, L. Dai, X. Ren, F. Ji, Q. Sun, Y. Zhang and L. Ci, *Energy Environ. Sci.*, 2021, **14**, 424–436.
42 J. Wu, Q. Kuang, K. Zhang, J. Feng, C. Huang, J. Li, Q. Fan, Y. Dong and Y. Zhao, *Energy Storage Mater.*, 2021, **41**, 297–309.
43 X. Yang, W. Deng, M. Chen, Y. Wang and C. F. Sun, *Adv. Mater.*, 2020, **32**, 2003592.
44 M. Yan, P. He, Y. Chen, S. Wang, Q. Wei, K. Zhao, X. Xu, Q. An, Y. Shuang, Y. Shao, K. T. Mueller, L. Mai, J. Liu and J. Yang, *Adv. Mater.*, 2018, **30**, 1703725.
45 T. Steiner, *Angew. Chem., Int. Ed.*, 2002, **41**, 48–76.
46 H. Yu, Y. D. Lin, S. L. Huang, X. X. Li, C. Sun and S. T. Zheng, *Angew. Chem., Int. Ed.*, 2023, **62**, e202302111.
47 D. A. Neamen, *Semiconductor Physics and Devices*, Publishing House of Electronics Industry, 2011.
48 C. Xu, J. Zhao, Y. A. Wang, W. Hua, Q. fu, X. Liang, X. Rong, Q. Zhang, X. Guo, C. Yang, H. Liu, B. Zhong and Y. S. Hu, *Adv. Energy Mater.*, 2022, **12**, 2200966.
49 T. Wang, W. Gao, Y. Zhao, S. Wang and W. Huang, *J. Mater. Sci. Technol.*, 2024, **173**, 107–113.
50 Y. Dai, C. Zhang, J. Li, X. Gao, P. Hu, C. Ye, H. He, J. Zhu, W. Zhang, R. Chen, W. Zong, F. Guo, I. P. Parkin, D. J. L. Brett, P. R. Shearing, L. Mai and G. He, *Adv. Mater.*, 2024, **36**, e2310645.
51 (*a*) CCDC 2472756: Experimental Crystal Structure Determination, 2026, DOI: 10.5517/ccdc.csd.cc2p03b5; (*b*) CCDC 2485510: Experimental Crystal Structure Determination, 2026, DOI: 10.5517/ccdc.csd.cc2pfcr8.